



# Detection of Carbon Monoxide’s 4.6 Micron Fundamental Band Structure in WASP-39b’s Atmosphere with JWST NIRSpec G395H

David Grant<sup>1</sup> , Joshua D. Lothringer<sup>2</sup> , Hannah R. Wakeford<sup>1</sup> , Munazza K. Alam<sup>3</sup> , Lili Alderson<sup>1</sup> , Jacob L. Bean<sup>4</sup> , Björn Benneke<sup>5</sup> , Jean-Michel Désert<sup>6</sup> , Tansu Daylan<sup>7,31</sup> , Laura Flagg<sup>8</sup> , Renyu Hu<sup>9,10</sup> , Julie Inglis<sup>10</sup> , James Kirk<sup>11</sup> , Laura Kreidberg<sup>12</sup> , Mercedes López-Morales<sup>13</sup> , Luigi Mancini<sup>12,14,15</sup> , Thomas Mikal-Evans<sup>12</sup> , Karan Molaverdikhani<sup>16,17</sup> , Enric Pallé<sup>18,19</sup> , Benjamin V. Rackham<sup>20,21,32</sup> , Seth Redfield<sup>22</sup> , Kevin B. Stevenson<sup>23</sup> , Jeff A. Valenti<sup>24</sup> , Nicole L. Wallack<sup>3</sup> , Keshav Aggarwal<sup>25</sup> , Eva-Maria Ahrer<sup>26,27</sup> , Ian J. M. Crossfield<sup>28</sup> , Nicolas Crouzet<sup>29</sup> , Nicolas Iro<sup>30</sup> , Nikolay K. Nikolov<sup>24</sup> , and Peter J. Wheatley<sup>26,27</sup>

(JWST Transiting Exoplanet Community ERS team)

<sup>1</sup> University of Bristol, HH Wills Physics Laboratory, Tyndall Avenue, Bristol, UK; [david.grant@bristol.ac.uk](mailto:david.grant@bristol.ac.uk)

<sup>2</sup> Department of Physics, Utah Valley University, Orem, UT 84058, USA

<sup>3</sup> Earth and Planets Laboratory, Carnegie Institution for Science, Washington, DC, USA

<sup>4</sup> Department of Astronomy & Astrophysics, University of Chicago, Chicago, IL, USA

<sup>5</sup> Department of Physics and Institute for Research on Exoplanets, Université de Montréal, Montreal, QC, Canada

<sup>6</sup> Anton Pannekoek Institute for Astronomy, University of Amsterdam, Amsterdam, The Netherlands

<sup>7</sup> Department of Astrophysical Sciences, Princeton University, Princeton, NJ, USA

<sup>8</sup> Department of Astronomy and Carl Sagan Institute, Cornell University, Ithaca, NY, USA

<sup>9</sup> Astrophysics Section, Jet Propulsion Laboratory, California Institute of Technology, Pasadena, CA, USA

<sup>10</sup> Division of Geological and Planetary Sciences, California Institute of Technology, Pasadena, CA, USA

<sup>11</sup> Department of Physics, Imperial College London, London, UK

<sup>12</sup> Max Planck Institute for Astronomy, Heidelberg, Germany

<sup>13</sup> Center for Astrophysics | Harvard & Smithsonian, Cambridge, MA, USA

<sup>14</sup> Department of Physics, University of Rome “Tor Vergata,” Rome, Italy

<sup>15</sup> INAF—Turin Astrophysical Observatory, Pino Torinese, Italy

<sup>16</sup> University Observatory Munich, Ludwig Maximilian University, Munich, Germany

<sup>17</sup> Exzellenzcluster Origins, Garching, Germany

<sup>18</sup> Instituto de Astrofísica de Canarias (IAC), E-38200 La Laguna, Tenerife, Spain

<sup>19</sup> Departamento de Astrofísica, Universidad de La Laguna (ULL), E-38206 La Laguna, Tenerife, Spain

<sup>20</sup> Department of Earth, Atmospheric and Planetary Sciences, Massachusetts Institute of Technology, Cambridge, MA 02139, USA

<sup>21</sup> Kavli Institute for Astrophysics and Space Research, Massachusetts Institute of Technology, Cambridge, MA 02139, USA

<sup>22</sup> Astronomy Department and Van Vleck Observatory, Wesleyan University, Middletown, CT, USA

<sup>23</sup> Johns Hopkins APL, Laurel, MD, USA

<sup>24</sup> Space Telescope Science Institute, Baltimore, MD, USA

<sup>25</sup> Indian Institute of Technology Indore, India

<sup>26</sup> Centre for Exoplanets and Habitability, University of Warwick, Coventry, UK

<sup>27</sup> Department of Physics, University of Warwick, Coventry, UK

<sup>28</sup> Department of Physics and Astronomy, University of Kansas, Lawrence, KS, USA

<sup>29</sup> Leiden Observatory, University of Leiden, Leiden, The Netherlands

<sup>30</sup> Institute for Astrophysics, University of Vienna, Vienna, Austria

Received 2023 January 5; revised 2023 April 21; accepted 2023 April 23; published 2023 May 23

## Abstract

Carbon monoxide (CO) is predicted to be the dominant carbon-bearing molecule in giant planet atmospheres and, along with water, is important for discerning the oxygen and therefore carbon-to-oxygen ratio of these planets. The fundamental absorption mode of CO has a broad, double-branched structure composed of many individual absorption lines from 4.3 to 5.1  $\mu\text{m}$ , which can now be spectroscopically measured with JWST. Here we present a technique for detecting the rotational sub-band structure of CO at medium resolution with the NIRSpec G395H instrument. We use a single transit observation of the hot Jupiter WASP-39b from the JWST Transiting Exoplanet Community Early Release Science (JTEC ERS) program at the native resolution of the instrument ( $R \sim 2700$ ) to resolve the CO absorption structure. We robustly detect absorption by CO, with an increase in transit depth of  $264 \pm 68$  ppm, in agreement with the predicted CO contribution from the best-fit model at low resolution. This detection confirms our theoretical expectations that CO is the dominant carbon-bearing molecule in WASP-39b’s atmosphere and further supports the conclusions of low C/O and supersolar metallicities presented in the JTEC ERS papers for WASP-39b.

*Unified Astronomy Thesaurus concepts:* Exoplanet atmospheres (487); Transmission spectroscopy (2133); Near infrared astronomy (1093)

<sup>31</sup> LSSTC Catalyst Fellow.

<sup>32</sup> 51 Pegasi b Fellow.



## 1. Introduction

JWST observations of exoplanet atmospheres have started to reveal absorption by carbon- and oxygen-bearing species at unprecedented precision. Recent measurements of the Saturn-mass hot Jupiter WASP-39b (Faedi et al. 2011) showed the definitive detection of carbon dioxide (CO<sub>2</sub>; Alderson et al. 2023; Rustamkulov et al. 2023; The JWST Transiting Exoplanet Community Early Release Science Team et al. 2023) and water (H<sub>2</sub>O; Ahrer et al. 2023; Alderson et al. 2023; Feinstein et al. 2023; Rustamkulov et al. 2023), with additional absorption from photochemically generated SO<sub>2</sub> (Tsai et al. 2022; Alderson et al. 2023; Rustamkulov et al. 2023). The low-resolution,  $R \sim 100$ , Near Infrared Spectrograph (NIRSpec) PRISM observations additionally hinted at the presence of broadband absorption due to carbon monoxide (CO; Rustamkulov et al. 2023). However, the broad absorption structure of CO was unable to be robustly confirmed by the initial evaluation of the higher-resolution NIRSpec G395H data when binned to  $R \sim 600$ , likely due to blending of absorption from CO<sub>2</sub>, H<sub>2</sub>O, cloud opacity, and other high-resolution molecular lines (Alderson et al. 2023).

In hot dense atmospheres, like those of hot Jupiters, carbon is distributed between CO and CO<sub>2</sub> if  $C/O \lesssim 1$ , with CO expected to be the dominant carbon-bearing molecule (Lodders & Fegley 2002; Heng & Lyons 2016). CO has been detected in the atmospheres of substellar objects at high resolution from the ground for both transiting and nontransiting exoplanets (e.g., Snellen et al. 2010; de Kok et al. 2013; Brogi et al. 2014; Giacobbe et al. 2021; Line et al. 2021) via direct imaging using a series of different methods (e.g., Konopacky et al. 2013; Barman et al. 2015; Schwarz et al. 2015; Snellen et al. 2015; Hoeijmakers et al. 2018; Petit dit de la Roche et al. 2018) and in brown dwarf atmospheres (e.g., Cushing et al. 2005). CO has also been seen in the upper atmospheres of all the solar system’s giant planets (Lodders & Fegley 1998; Encrenaz et al. 2004). More recently JWST spectra of the directly imaged and relatively isolated giant exoplanet VHS 1256b (Miles et al. 2022) revealed the characteristic CO banding structure at 2.3 and 4.6  $\mu\text{m}$  using JWST’s NIRSpec integral field unit, showing that it is possible to detect CO at these wavelengths and resolutions.

Here we present a novel method to detect the fundamental ( $\nu = 1-0$ ) band structure of CO at 4.6  $\mu\text{m}$  in the transmission spectrum of the hot Jupiter WASP-39b. Throughout this work we refer to the clusters of individual lines that make up the rovibrational band structure as sub-bands.

## 2. JWST Observations

Multiple transits of WASP-39b were observed by JWST as part of the Directors Discretionary Early Release Science (ERS) program (ERS-1366; PIs: N. M. Batalha, J. Bean, and K. B. Stevenson) in 2022 July (Stevenson et al. 2016; Bean et al. 2018). Of these observations, a single transit was observed using JWST’s NIRSpec with the G395H grating (Birkmann et al. 2022; Jakobsen et al. 2022). This mode captures time-series spectra with a resolving power of  $R \sim 2700$  (or  $\sim 6.6 \text{ \AA pixel}^{-1}$ ) and a wavelength range from 2.75 to 5.16  $\mu\text{m}$ , making this observation well suited to analyzing the transmission spectrum of CO in higher resolution than ever before from space. This data set is comprised of 465 integrations, each

made up of 70 groups, and sums to a total exposure duration of 8.3 hr. This setup provides full coverage of the 2.8 hr transit event, as well as ample monitoring of the star’s baseline flux pre- and post-transit.

NIRSpec’s G395H grating disperses light across two adjacent detectors, NRS1 and NRS2, with a small  $\sim 0.1 \mu\text{m}$  gap at 3.8  $\mu\text{m}$ . In search of CO signals, we focus our analysis on data longward of 3.8  $\mu\text{m}$ , that is, using data solely from the NRS2 detector. We reduce these data using a combination of the JWST Science Calibration Pipeline (v1.6.2, Bushouse et al. 2022) and custom open-source routines (v0.1-beta, Alderson et al. 2022). Following the JWST pipeline conventions, the data reduction, from raw data files to stellar spectra, is separated into two stages<sup>33,34</sup> and is followed by light-curve fitting.

In stage 1 we largely utilize the JWST pipeline’s default processing steps. However, we skip the dark-current step owing to the present quality of available reference files. Additionally, after the jump-detection step is run, we “desstripe” the data at the group level. Desstriping involves subtracting the column-by-column median background value from each column’s pixels. This aims to reduce the  $1/f$  noise at timescales longer than the column read time, or 440  $\mu\text{s}$ , and is more effective when corrected for at the group level (Rustamkulov et al. 2023; The JWST Transiting Exoplanet Community Early Release Science Team et al. 2023). These median values are computed with pixels having been flagged for poor data quality removed; and in particular, flagged pixels are made maximally consistent across groups within an integration. This flagging procedure ensures the same set of pixels are masked within a given pixel’s ramp, and we find this improves ramp continuity in the presence of transient outliers such as cosmic ray hits. After desstriping, the default ramp-fitting step is run, and rate images are output from stage 1.

In stage 2 we utilize custom routines to clean the rate images and extract a time series of stellar spectra. Outlier cleaning is performed by finding deviations from an estimated spatial profile, as is common in optimal extraction (Horne 1986). However, the curved spectral trace means the spatial profile must be created piecewise from windowed row-wise polynomial fits, as has been similarly utilized by Zhang et al. (2021). We find a window size of 100 pixels, a polynomial order of 4, and an outlier threshold set at 4 standard deviations are sufficient to clean the curved spectral trace. Next, the background is subtracted column by column, and the outlier cleaning is repeated once more. Stellar spectra are extracted using a box aperture centered on the spectral trace and with a width of 6 times the measured standard deviation of the point-spread function. The resulting stellar spectra are comprised of between  $\sim 90,000$  and  $\sim 20,000$  electrons per column, decreasing from the short- to long-wavelength side of the NRS2 detector.

### 2.1. Transmission Spectrum

From the stellar spectra, we generate a transmission spectrum at the highest resolution possible to maximize our chances of detecting the fine structure of the CO absorption band. To achieve this, we make spectroscopic light curves at

<sup>33</sup> Stage 1: processes 4D uncalibrated data into 3D rate images.

<sup>34</sup> Stage 2: processes 3D rate images into 2D stellar spectra.

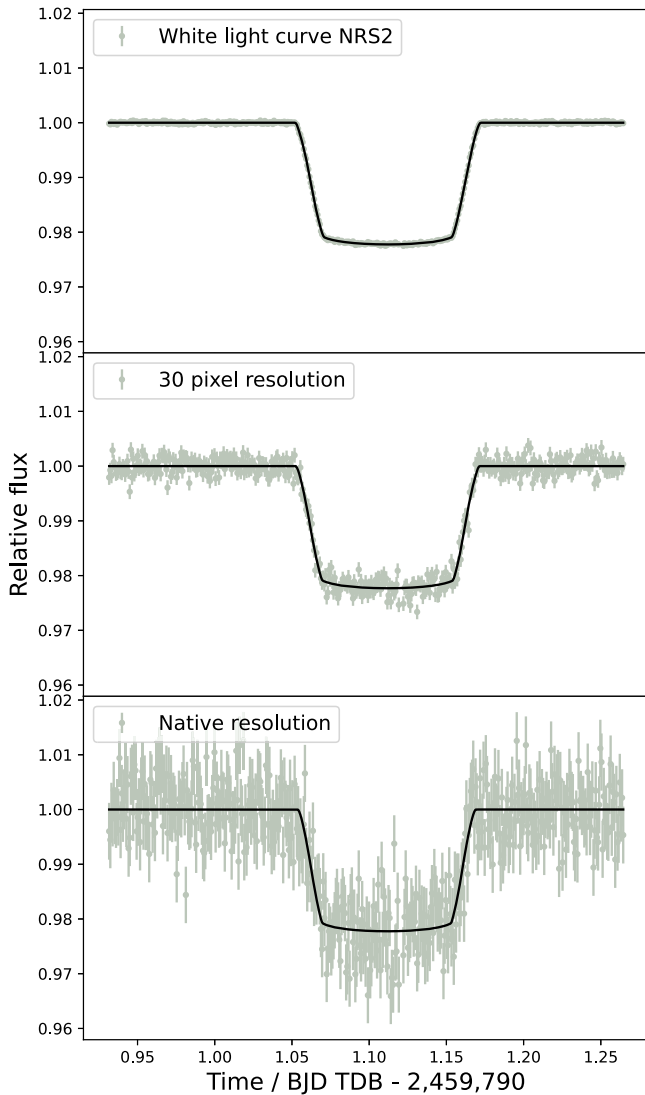


**Figure 1.** Fits to the white light curve as well as example fits, centered on  $4.7\mu\text{m}$ , to spectroscopic light curves at 30 pixels and native resolution. Shown are the corrected fluxes after the systematics model has been removed.

the native resolution of NIRSpect’s G395H mode; these bins are just 2 pixels wide. For comparison, we also fit spectroscopic light curves with bins 30 pixels wide, as well as fit the entire NRS2 white light curve (see Figure 1). The light curves and transmission spectrum presented in Alderson et al. (2023) consisted of bins 10 pixels wide.

The data quality is such that systematics are barely visible in the raw light curves, with the exception of a small exponential ramp over the first  $\sim 10$  integrations, and a mirror tilt event at integration 269, as seen by Alderson et al. (2023). The exponential ramp is removed by discarding the first 15 integrations to ensure the full ramp effect does not impact the measured stellar baseline. The tilt event is accounted for by normalizing the pre- and post-tilt flux by the pre- and post-transit median flux, respectively. We also discard three integrations immediately surrounding the tilt event. Any remaining systematics are modeled by linear regression of the measured relative positions of the spectral trace. These positions are found by cross correlation in the dispersion direction using the median stellar spectra and in the cross-dispersion direction using the median point-spread function.

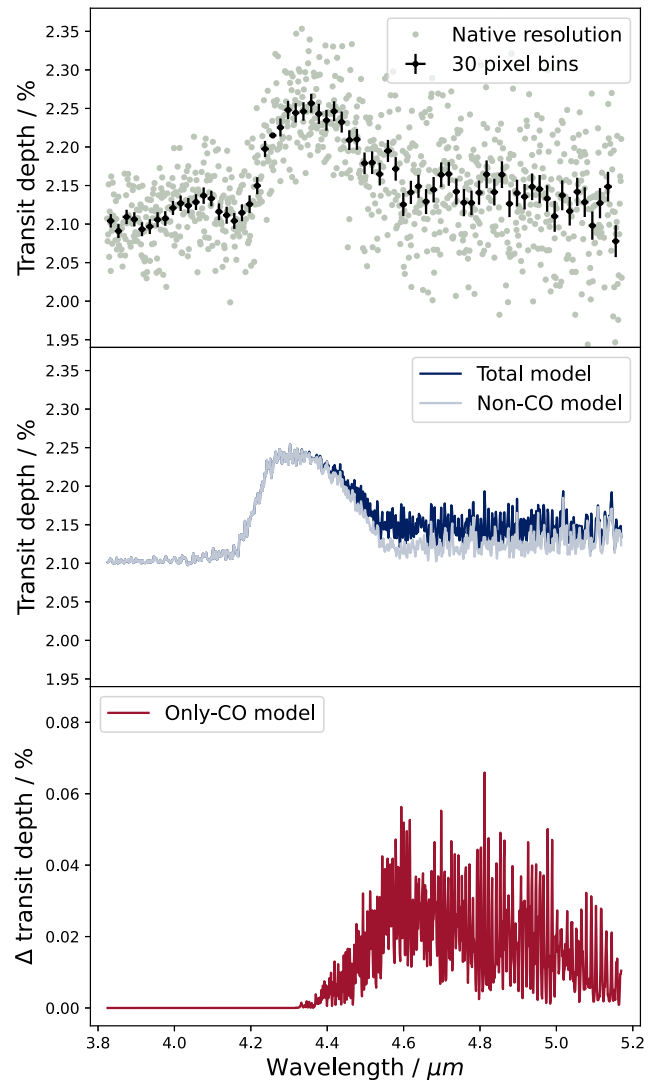


**Figure 2.** Top panel: observed transmission spectra at native resolution (light green) and at 30 pixel resolution (black). Middle panel: model transmission spectrum fit to the data (dark blue) and the same model but with CO removed (gray). Bottom panel: model contribution from CO only (red).

The total light-curve model,  $f(t)$ , is described by

$$f(t) = T(t, \theta) + \sum_{j \in W} f_{0,j} + S_j(x_j, y_j), \quad (1)$$

where

$$S_j(x_j, y_j) = p_{1,j}x_j + p_{2,j}y_j. \quad (2)$$

Here,  $T$  is the physical transit model as a function of time,  $t$ , and transit parameter vector,  $\theta$ .  $f_0$  is an offset to the baseline flux.  $S_j$  is the systematics model as a linear function of the spectral trace positions,  $x_j$  and  $y_j$ . We elect to fit the nonphysical model components piecewise, either side of the tilt event, where each window of data is denoted by the subscript  $j$  from the set  $W = \{\text{pre} - \text{tilt}, \text{post} - \text{tilt}\}$ . The  $x_j$  and  $y_j$  traces can be seen in Alderson et al. (2023, extended data Figures 1 and 2), and for computational efficiency the values are standardized by subtracting their means and dividing by their standard deviations, independently for each  $j$ . For  $T$  we use a Batman transit model (Kreidberg 2015) with a fixed, nonlinear, four-

parameter limb-darkening law computed using ExoTiC-LD (Grant & Wakeford 2022) for each spectral bin using the 3D Stagger-grid of stellar models (Magic et al. 2015).

We perform fitting of our light-curve model with a least-squares optimizer (Virtanen et al. 2020), using the Levenberg–Marquadt algorithm (Moré 1978), cofitting the parameters  $\theta$ ,  $f_{0,j}$ ,  $p_{1,j}$ , and  $p_{2,j}$  simultaneously. We initially fit the white light curve to find the best-fit values for the center of transit time,  $t_0 = 2,459,791.112128 \pm 0.000021$  BJD<sub>TDB</sub>; semimajor axis,  $a = 11.395 \pm 0.028 R_*$ ; and inclination  $i = 87.759 \pm 0.028^\circ$ . These values are then fixed in the spectroscopic light-curve fits that follow. For each spectroscopic light-curve fit, the standard deviation of the residuals is used to inflate the original uncertainties on the fluxes, and then the fits are repeated. The uncertainties in the resulting transit depths are computed from the square root of the inverse Hessian matrix. We validate this fast approximation by using a Markov Chain Monte Carlo algorithm (Foreman-Mackey et al. 2013), with uniform priors, to sample the posterior distributions of several transit depths, and we find that the results are equivalent. These checks span the entire wavelength range of NRS2, with the inferred transit depths being on average 0.03 standard deviations discrepant and the corresponding uncertainties 1.7% different.

In Figure 1 we show fits to the white light curve, as well as example fits, centered on  $4.7 \mu\text{m}$ , to spectroscopic light curves at 30 pixels and native resolution. In each panel, we show the corrected flux values with the systematics model removed. The systematics model accounts for on average 1.3% of the residual variance although close inspection of the light curves indicates a small amount of correlated noise remains. Tests varying the width of the spectral bins reveal the variance in the light curves becomes closer to the expected photon noise for narrower bins. This is indicative of the remaining noise being spatially correlated on the detector, most likely due to a small amount of leftover uncleaned  $1/f$  noise. There is also likely some minor time-correlated noise, most clearly seen at the 30 pixel resolution; however, we were unable to identify the origin of this noise. The mean residual standard deviations are 163 ppm, 1260 ppm, and 4644 ppm for the white light, 30 pixel, and native-resolution light-curve fits, respectively. At native resolution this precision corresponds to  $1.1 \times$  photon noise. In the top panel of Figure 2 we show the transmission spectrum.

### 3. Theoretical Models

To investigate the presence of CO in the transmission spectrum of WASP-39b, we fit the observations to a grid of PHOENIX atmosphere models (Hauschildt et al. 1999; Barman et al. 2001; Lothringer & Barman 2020). This was the same grid used in the initial investigation of WASP-39b’s G395H spectrum in Alderson et al. (2023). The grid is sampled every Angstrom and explores the irradiation temperature (i.e., absorbed heat from the star,  $T_{\text{irr}} = 1020, 1120, \text{ and } 1220$  K, respectively), internal temperature ( $T_{\text{int}} = 200$  and  $400$  K), metallicity ( $0.1\times, 1\times, 10\times, 50\times, \text{ and } 100\times$  solar; Asplund et al. 2009), C/O ratio ( $0.3, 0.54$  (solar),  $0.7, \text{ and } 1.0$ ), and the presence of aerosols (a cloud deck at  $0.3, 1, 3, \text{ and } 10$  mbar or a Rayleigh-scattering haze at  $10\times$  the  $\text{H}_2$  scattering cross section). We also included models with rainout chemistry (i.e., abundances of refractory elements are depleted in the layers above which they condense) compared to pure chemical equilibrium. Disequilibrium abundances of  $\text{SO}_2$  from photochemistry (Tsai et al. 2022) were not included in these models.

Species in the opacity calculation include CH,  $\text{CH}_4$ , CN, CO,  $\text{CO}_2$ ,  $\text{C}_2$ ,  $\text{C}_2\text{H}_2$ ,  $\text{C}_2\text{H}_4$ ,  $\text{C}_2\text{H}_6$ , CaH, CrH, FeH, HCN, HCl, HF, HI, HDO,  $\text{HO}_2$ ,  $\text{H}_2$ ,  $\text{H}_2\text{S}$ ,  $\text{H}_2\text{O}$ ,  $\text{H}_2\text{O}_2$ ,  $\text{H}_3^+$ , MgH, NH,  $\text{NH}_3$ , NO,  $\text{N}_2$ ,  $\text{N}_2\text{O}$ , OH,  $\text{O}_2$ ,  $\text{O}_3$ ,  $\text{PH}_3$ ,  $\text{SF}_6$ , SiH, SiO,  $\text{SiO}_2$ , TiH, TiO, VO, and atoms up to U. Of relevance for this work, we use the high-temperature CO line list from Goorvitch (1994) that was used for the PHOENIX grid in Alderson et al. (2023), but we also test against the newer Li et al. (2015) list.

Our best-fit model at low resolution, which we take to be our fiducial model, has  $f = 0.351$ ,  $T_{\text{int}} = 200$  K,  $10\times$  solar metallicity,  $\text{C/O} = 0.3$ , a cloud deck at  $0.3$  mbar, no hazes, and rainout chemistry. These results are mostly consistent with those found using the median reduced G395H spectrum from 11 different analyses in Alderson et al. (2023), except for the internal temperature (200 versus  $400$  K) and the preference for rainout chemistry, both of which have relatively minor effects in the wavelength region probed by these G395H observations. We attribute this nonstatistically significant difference to the minor differences between data reductions.

We show the best-fit model compared to 30 pixel wide bins of the observations in the middle panel of Figure 2. Absorption from  $\text{SO}_2$  at  $4.0 \mu\text{m}$  and  $\text{CO}_2$  at  $4.3 \mu\text{m}$  are seen in the data, as previously described in Tsai et al. (2022), Alderson et al. (2023), Rustamkulov et al. (2023), and The JWST Transiting Exoplanet Community Early Release Science Team et al. (2023). The middle panel also shows the model with and without the CO opacity. The difference of these two models is plotted in the bottom panel, indicating the contribution of CO to the best-fit transit spectrum. At the low effective resolution of 30 pixel bins, the presence of CO in the G395H spectrum is not apparent, and its detection was not statistically justified due to blending with non-CO opacities like  $\text{H}_2\text{O}$ ,  $\text{CO}_2$ , and the cloud opacity (Alderson et al. 2023).

### 4. Defining CO Sub-bands

In order to detect the high-resolution features of CO, we define a set of wavelengths that are theorized to either display CO absorption (hereafter in-band) or not to display CO absorption (hereafter out-of-band). The aim is to compare the transit depths from each set and thereby probe CO’s fundamental band structure. This method is displayed graphically in Figure 3. This plot shows how at the resolution of the G395 mode we are able to probe small clusters of CO lines, which together we refer to as sub-bands.

We set out to define these sub-bands such that they represent a good contrast between the in- versus out-of-band transit depth and furthermore, are not biased toward finding other potential species’ high-resolution signals included in the atmospheric models. As we are concerned only with the high-resolution structure, we consider these sub-bands relative to the continuum level. We also restrict our analysis to the wavelength interval  $4.4 \mu\text{m} < \lambda < 5.0 \mu\text{m}$  as this is the region that optimizes the balance between the observed signal-to-noise and the amplitude of the model’s high-resolution CO structure. In this region, the resolving power of the G395 mode ranges from  $R \sim 3040$  to  $\sim 3516$  with increasing wavelength.

Now, with the models for only-CO and non-CO in hand from Section 3, we lay out a method for defining clear CO sub-bands. For each model, we remove the continuum with a Savitzky–Golay filter (Savitzky & Golay 1964) and then standardize the mean and standard deviation of the model transit depths. To define the clear in-band wavelengths,  $\Lambda_{\text{CO-in}}$ ,

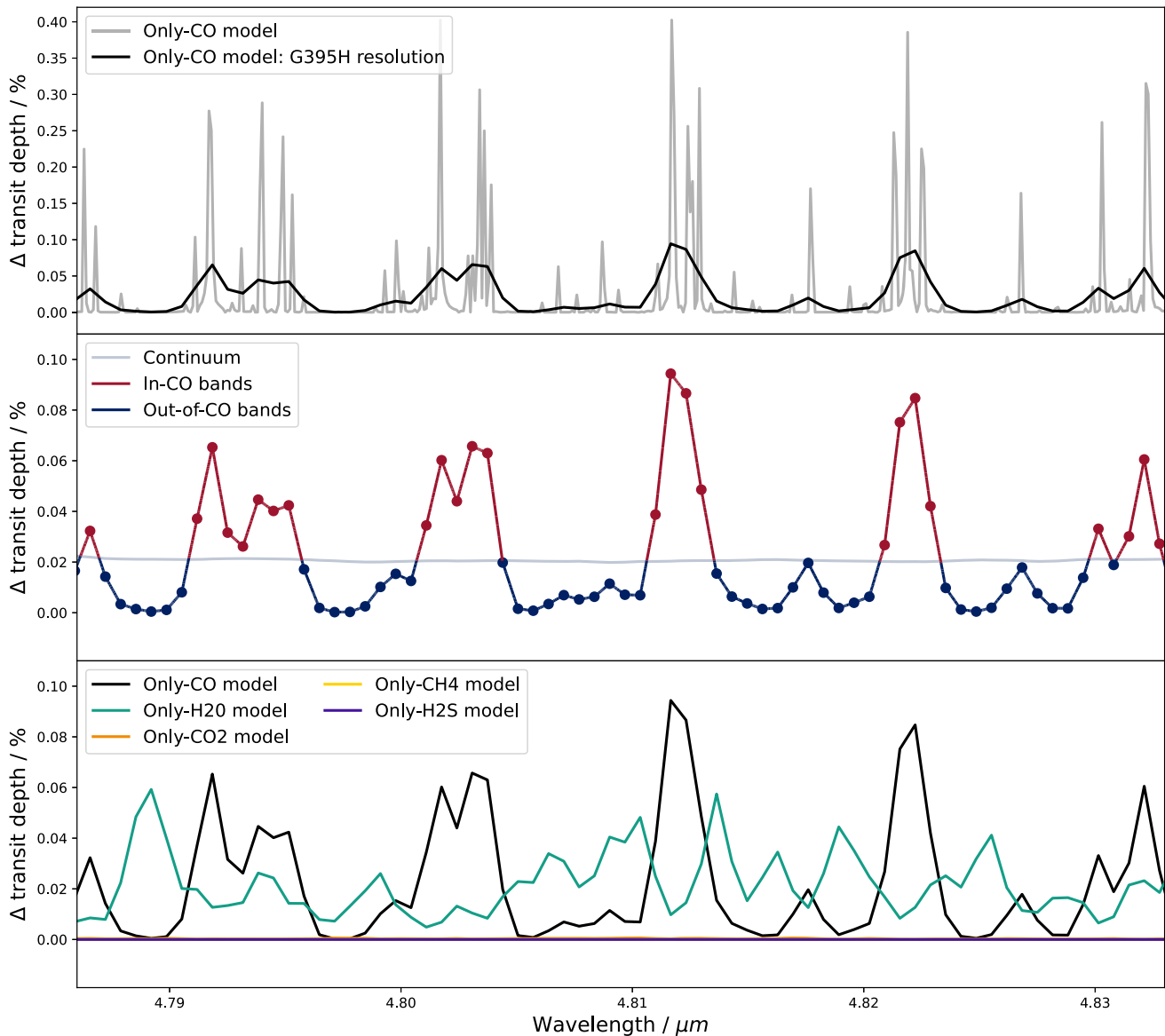


**Figure 3.** Top panel: example wavelength sector showing the model contribution from CO only. The model is shown at simulated resolution (gray, sampled every Ångström) and after being convolved with the observed point-spread function and rebinned onto the detector’s wavelength grid (black). Middle panel: visualization of our method for detecting CO sub-band structure. Red and blue portions indicate wavelengths that are in-band or out-of-band, respectively. Note these wavelength selections are refined in Figure 4. Bottom panel: model contributions per molecule, where H<sub>2</sub>O is the only significant molecular absorber in this wavelength sector other than CO.

we select the only-CO model transit depths above a set threshold but only where these wavelengths do not show appreciable signals in the non-CO model. To define the clear out-of-band wavelengths,  $\Lambda_{\text{CO-out}}$ , we use the same logic but for only-CO model points below a set threshold. In this way, the sub-bands will probe the highest contrast regions of the CO signal without inadvertently confusing the CO signal with other species. In terms of logical operators we can write

$$\Lambda_{\text{CO-in}} = X_{\text{in}} \text{ AND } (\text{NOT } (Y_{\text{in}} \text{ OR } Y_{\text{out}})), \quad (3)$$

$$\Lambda_{\text{CO-out}} = X_{\text{out}} \text{ AND } (\text{NOT } (Y_{\text{in}} \text{ OR } Y_{\text{out}})), \quad (4)$$

where  $X_{\text{in}}$  and  $X_{\text{out}}$  are wavelengths with only-CO model transit depths above and below set thresholds, and  $Y_{\text{in}}$  and  $Y_{\text{out}}$  are wavelengths with non-CO model transit depths above and below set thresholds, respectively.

As a graphical description, we display the selected wavelengths in Figure 4. Here, the clear in- and out-of-band

wavelengths are shown in the right-hand panel. We set the threshold values to  $\pm 0.3$  for  $X$  and to  $\pm 2.0$  for  $Y$ . The motivation for these threshold values is to balance the contrast of transit depth between in-band and out-of-band versus the number of bands included in the samples and thus the statistical power of any detection test. These thresholds result in 259 clear bands, of which 111 are in-band and 148 are out-of-band. The distribution of the number of contiguous pixels in-band has a mean of 3.0 pixels and a standard deviation of 1.1 pixels. The distribution for out-of-band has a mean of 3.8 pixels and a standard deviation of 1.7 pixels.

## 5. Detecting CO Sub-bands

Using our definition of CO sub-bands, we categorize the transit depths from the observed native-resolution transmission spectrum as either in-band or out-of-band. This process generates two samples of transit depths, one for each of the

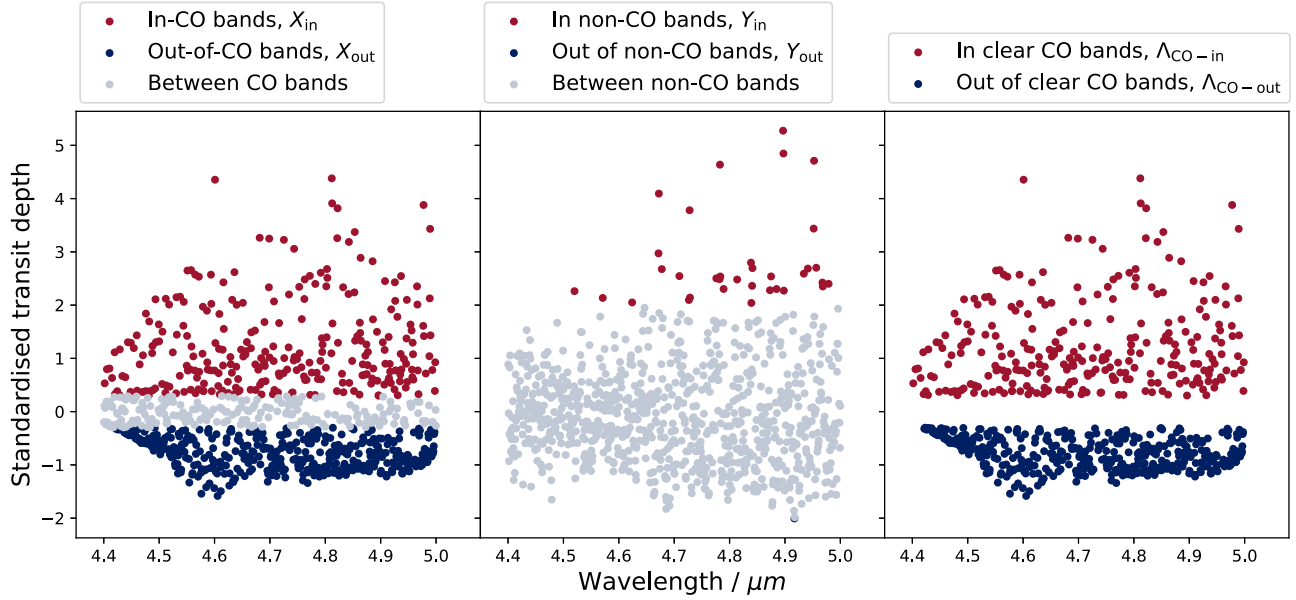


**Figure 4.** Graphical representation of the logic behind our in-band (red) and out-of-band (dark blue) definitions. The panels show the cuts in the models for the only-CO model (left-hand panel), the non-CO model (middle panel), and the resulting clear CO sub-bands model (right-hand panel).

theorized underlying populations of transit depth for in-band and out-of-band. As in Section 4, we remove the continuum from the observed transit depths to probe only the high-resolution CO features. We display these two samples in the top panel of Figure 5. The CO in-band sample,  $\delta(\Lambda_{\text{CO-in}})$ , has a mean,  $\mu_{\text{in}} = 21,616$  ppm, and standard deviation,  $\sigma_{\text{in}} = 501$  ppm. The CO out-of-band sample,  $\delta(\Lambda_{\text{CO-out}})$ , has a mean,  $\mu_{\text{out}} = 21,352$  ppm, and standard deviation,  $\sigma_{\text{out}} = 576$  ppm.

To test statistically if the in-band sample displays greater CO absorption than the out-of-band sample, we conduct a hypothesis test. We run a two-sample T-test, specifically a one-tailed Welch’s t-test (Welch 1947), with the following hypothesis:

$$\mathcal{H}_0 : \mu_{\text{in}} = \mu_{\text{out}}, \quad (5)$$

$$\mathcal{H}_1 : \mu_{\text{in}} > \mu_{\text{out}}, \quad (6)$$

where  $\mathcal{H}_0$  and  $\mathcal{H}_1$  are the null and alternate hypotheses, respectively. Running this test on our samples, we find a statistically significant result. The in-band samples have a greater mean transit depth than the out-of-band samples, with  $t = 3.90$  and  $p = 0.00006$ , and hence, we detect high-resolution CO band structure with assurance.

As a visual representation, we plot the sampling distributions of the mean transit depths in the middle panel of Figure 5. The sampling distributions are normally distributed such that

$$\bar{\delta}(\Lambda_{\text{CO-in}}) \sim \mathcal{N}\left(\mu_{\text{in}}, \frac{\sigma_{\text{in}}^2}{n_{\text{in}}}\right), \quad (7)$$

$$\bar{\delta}(\Lambda_{\text{CO-out}}) \sim \mathcal{N}\left(\mu_{\text{out}}, \frac{\sigma_{\text{out}}^2}{n_{\text{out}}}\right), \quad (8)$$

where the standard errors are  $\sigma_{\text{in}}/n_{\text{in}}^{1/2} = 48$  ppm and  $\sigma_{\text{out}}/n_{\text{out}}^{1/2} = 48$  ppm, and the sample sizes are given by  $n_{\text{in}}$  and  $n_{\text{out}}$ . The difference between the transit depth means is  $264 \pm 68$  ppm. This difference, in terms of the resulting light-curve models, is displayed in the bottom panel of Figure 5.

In addition to this result, we conduct sensitivity tests for the  $X$  and  $Y$  thresholds set in Section 4. We find that our results are not sensitive to the  $Y$  threshold, but when varying the  $X$  threshold we observe a change in the detected transit-depth difference between in-band and out-of-band samples. As the  $X$  threshold increases, the transit-depth difference increases but with increasing uncertainty owing to the reduced statistical power. For example, if the  $X$  threshold values are increased to  $\pm 0.4$ , the difference between the transit-depth means becomes  $301 \pm 81$  ppm. Intuitively, this effect can be understood as the larger thresholds narrowing in on the peaks of the CO sub-bands, where the contrast in transit depth is greater but fewer data points lie.

## 6. Discussion

The technique presented works particularly well with JWST’s NIRSpc G395H mode, owing to its comparatively high spectral resolution. Given this resolution, it was vital in our analysis to account for the Doppler transformations of both the barycentric velocity of the WASP-39 system,  $\gamma_{*} = -58.4421 \text{ km s}^{-1}$  (Mancini et al. 2018), and of JWST’s barycentric velocity at the time of observation,  $\gamma_{\text{JWST}} = -28.88807 \text{ km s}^{-1}$ . In fact, the robustness of our detection is further backed up by trialing spurious Doppler transformations. We find that shifting our models by velocities equivalent to just one resolution element ( $\pm 88 \text{ km s}^{-1}$  at  $4.5 \mu\text{m}$ ) in either direction leads to nondetections, with  $p = 0.42$  and  $0.17$ . This further highlights the fidelity and soundness of our detection while also underscoring the need for models applied to the highest-resolution JWST modes to be appropriately Doppler shifted when searching for narrow molecular features.

Our technique offers an independent test for the presence of molecular features in the atmospheres of exoplanets for well-characterized molecules with precise line lists. Differences in the measured excess transit depth of only 4 ppm were found using the different CO line lists of Goorvitch (1994) and Li et al. (2015) though such differences may be greater in the

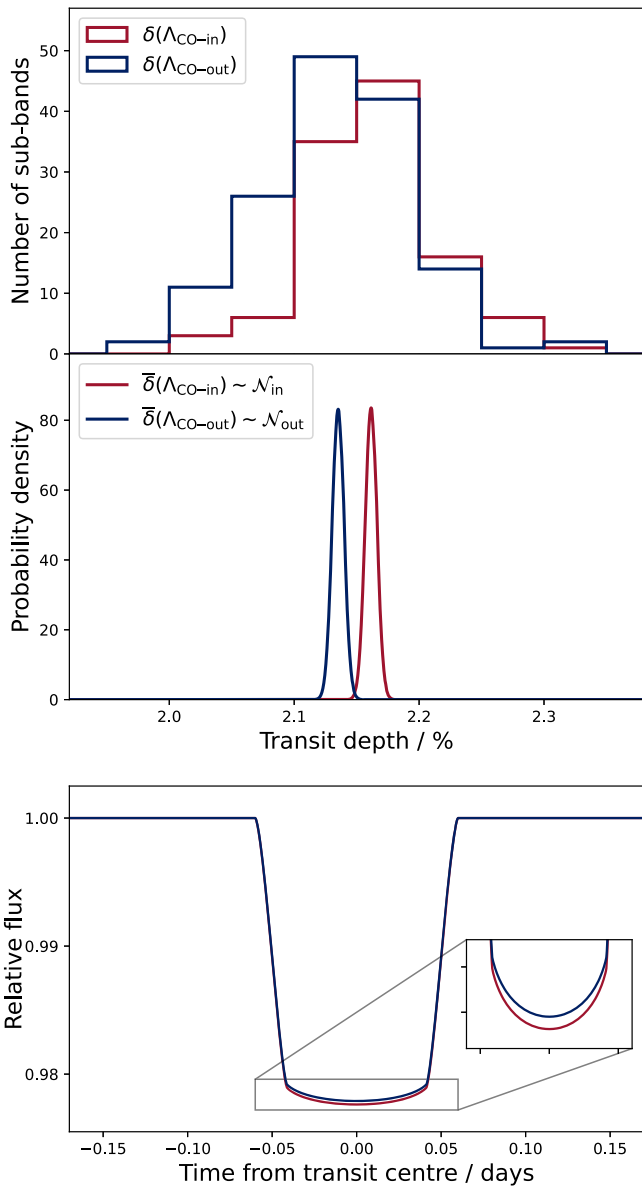


**Figure 5.** Top panel: samples showing the number of sub-bands as a function of transit depth,  $\delta$ , for in- and out-of-band CO. Middle panel: sampling distributions of the mean transit depths,  $\bar{\delta}$ , for in- and out-of-band CO. These sampling distributions are modeled as Gaussians with means and standard deviations inferred from the measured samples shown in the top panel. Bottom panel: light-curve models visualizing the measured difference in transit depth for in- and out-of-band CO.

overtone bands where the two lists disagree more than in the fundamental band. The technique may be applied to other molecules with rotational sub-band structures distinctly separated at  $R \sim 3000$ , for example  $\text{CH}_4$ ,  $\text{NH}_3$ , or  $\text{HCN}$  between 2.5 and 3.5  $\mu\text{m}$ , but the development and use of accurate and complete line lists for other species are necessary. The structure may be more difficult to measure for molecules such as  $\text{H}_2\text{O}$  that are more easily distinguished by their broadband structure due to the rovibrational lines being more tightly clustered.

Aside from the technique outlined in this work, cross-correlation methods, often used with high-resolution ground-based data, may also be applied to the highest-resolution JWST modes. Certain cross-correlation formalisms

(e.g., Brogi & Line 2019; Gibson et al. 2020) enable the construction of a likelihood function, which can also be used for the detection and retrieval of molecules and their abundances, and a future methodology comparison with traditional low-resolution methods may be fruitful.

## 7. Summary and Conclusions

We have detected absorption structure in CO’s fundamental band using JWST’s NIRSpec G395H mode. To make this detection we employed a new technique in which we categorized wavelength bins as either in-band or out-of-band and then compared the transit depths of the resulting samples. We found the mean transit depth of CO sub-bands to be  $264 \pm 68$  ppm larger than the transit depth between CO sub-bands. This value is in agreement with the prediction from the PHOENIX model spectrum of 217 ppm when using the same sub-bands.

While  $\text{CO}_2$ ’s opacity is much stronger per molecule in the G395H wavelength regime and was therefore more easily detected in Alderson et al. (2023), CO is actually by far the dominant carbon-bearing molecule throughout WASP-39b’s atmosphere with a 1 mbar volume mixing ratio in the best-fit model of 2326 ppm compared to 7 ppm of  $\text{CO}_2$ . This fact remains true for all giant planets in chemical equilibrium with plausible heavy-element enrichments (e.g.,  $M/H \leq 100x$  solar). Thus the detection of CO, in addition to  $\text{CO}_2$ , enables a more robust and complete understanding of a planet’s chemical inventory, especially with respect to the measurement of the C/O ratio. Without such a measurement, any inference of the bulk carbon abundance or C/O ratio from  $\text{CO}_2$  alone would rely on assumptions of chemical equilibrium. We can therefore not only be more confident in the detection of CO with JWST/NIRSpec/PRISM (Rustamkulov et al. 2023) but also in the conclusions from the other JWST spectra that WASP-39b has a subsolar to solar C/O ratio and likely formed interior to the  $\text{CO}_2$  ice line (Ahrer et al. 2023; Alderson et al. 2023; Feinstein et al. 2023).

We thank the two anonymous reviewers for helpful comments. We thank the JWST Transiting Exoplanet Community ERS team for their hard work on the proposal, observations, and data presented in this paper. We thank the JTEC ERS G395H sub-team for fruitful conversations. This work is based on observations made with the NASA/ESA/CSA JWST. The data were obtained from the Mikulski Archive for Space Telescopes at the Space Telescope Science Institute, which is operated by the Association of Universities for Research in Astronomy, Inc., under NASA contract NAS 5-03127 for JWST. These observations are associated with program JWST-ERS-01366. Support for program JWST-ERS-01366 was provided by NASA through a grant from the Space Telescope Science Institute. The specific observations analyzed can be accessed.<sup>35</sup> Science data processing version (SDP\_VER) 2022\_2a generated the uncalibrated data that we downloaded from MAST. We used JWST Calibration Pipeline software version (CAL\_VER) 1.6.2 with modifications described in the text. We used calibration reference data from context (CRDS\_CTX) 0930, except as noted in the text. D.G. acknowledges funding from the UKRI STFC Consolidated Grant ST/V000454/1. The data and

<sup>35</sup> doi:10.17909/1j77-6w13.

models associated with this study can be found in The JWST Transiting Exoplanet Community Early Release Science Program Zenodo Library.

Author Contributions: D.G. performed the data analysis with atmospheric models supplied by J.D.L.; D.G., J.D.L., and H.R.W. wrote the manuscript. D.G. and J.D.L. designed the analysis method in discussion with the ERS G395H sub-team led by H.R.W. and L.A. All other authors read and approved the manuscript. N.M.B., J.L.B., and K.B.S. provided overall program leadership of the JWST Transiting Exoplanet Community ERS program.

*Facility:* JWST(NIRSpec G395H).

*Software:* JWST pipeline (Bushouse et al. 2022), ExoTiC-JEDI (Alderson et al. 2022), ExoTiC-LD (Grant & Wakeford 2022), Batman (Kreidberg 2015), numpy (Harris et al. 2020), SciPy (Virtanen et al. 2020), matplotlib (Hunter 2007), pandas (pandas development team, T 2022), xarray (Hoyer & Hamman 2017; Hoyer et al. 2022), astropy (Astropy Collaboration et al. 2013, 2018; Price-Whelan et al. 2022).

### ORCID iDs

David Grant  <https://orcid.org/0000-0001-5878-618X>  
 Joshua D. Lothringer  <https://orcid.org/0000-0003-3667-8633>  
 Hannah R. Wakeford  <https://orcid.org/0000-0003-4328-3867>  
 Munazza K. Alam  <https://orcid.org/0000-0003-4157-832X>  
 Lili Alderson  <https://orcid.org/0000-0001-8703-7751>  
 Jacob L. Bean  <https://orcid.org/0000-0003-4733-6532>  
 Björn Benneke  <https://orcid.org/0000-0001-5578-1498>  
 Jean-Michel Désert  <https://orcid.org/0000-0002-0875-8401>  
 Tansu Daylan  <https://orcid.org/0000-0002-6939-9211>  
 Laura Flagg  <https://orcid.org/0000-0001-6362-0571>  
 Renyu Hu  <https://orcid.org/0000-0003-2215-8485>  
 Julie Inglis  <https://orcid.org/0000-0001-9164-7966>  
 James Kirk  <https://orcid.org/0000-0002-4207-6615>  
 Laura Kreidberg  <https://orcid.org/0000-0003-0514-1147>  
 Mercedes López-Morales  <https://orcid.org/0000-0003-3204-8183>  
 Luigi Mancini  <https://orcid.org/0000-0002-9428-8732>  
 Thomas Mikal-Evans  <https://orcid.org/0000-0001-5442-1300>  
 Karan Molaverdikhani  <https://orcid.org/0000-0002-0502-0428>  
 Enric Palle  <https://orcid.org/0000-0003-0987-1593>  
 Benjamin V. Rackham  <https://orcid.org/0000-0002-3627-1676>  
 Seth Redfield  <https://orcid.org/0000-0003-3786-3486>  
 Kevin B. Stevenson  <https://orcid.org/0000-0002-7352-7941>  
 Nicole L. Wallack  <https://orcid.org/0000-0003-0354-0187>  
 Keshav Aggarwal  <https://orcid.org/0000-0002-7004-8670>  
 Eva-Maria Ahrer  <https://orcid.org/0000-0003-0973-8426>  
 Nicolas Crouzet  <https://orcid.org/0000-0001-7866-8738>  
 Nicolas Iro  <https://orcid.org/0000-0003-2329-418X>  
 Nikolay K. Nikolov  <https://orcid.org/0000-0002-6500-3574>  
 Peter J. Wheatley  <https://orcid.org/0000-0003-1452-2240>

### References

Ahrer, E.-M., Stevenson, K. B., Mansfield, M., et al. 2023, *Natur*, 614, 653  
 Alderson, L., Grant, D., & Wakeford, H. 2022, Exo-TiC/ExoTiC-JEDI: v0.1-beta-release, v0.1, Zenodo, doi:10.5281/zenodo.7185855  
 Alderson, L., Wakeford, H. R., Alam, M. K., et al. 2023, *Natur*, 614, 664

Asplund, M., Grevesse, N., Sauval, A. J., & Scott, P. 2009, *ARA&A*, 47, 481  
 Astropy Collaboration, Price-Whelan, A. M., Sipőcz, B. M., et al. 2018, *AJ*, 156, 123  
 Astropy Collaboration, Robitaille, T. P., Tollerud, E. J., et al. 2013, *A&A*, 558, A33  
 Barman, T. S., Hauschildt, P. H., & Allard, F. 2001, *ApJ*, 556, 885  
 Barman, T. S., Konopacky, Q. M., Macintosh, B., & Marois, C. 2015, *ApJ*, 804, 61  
 Bean, J. L., Stevenson, K. B., Batalha, N. M., et al. 2018, *PASP*, 130, 114402  
 Birkmann, S., Ferruit, P., Giardino, G., et al. 2022, *A&A*, 661, A83  
 Brogi, M., de Kok, R. J., Birkby, J. L., Schwarz, H., & Snellen, I. A. G. 2014, *A&A*, 565, A124  
 Brogi, M., & Line, M. R. 2019, *AJ*, 157, 114  
 Bushouse, H., Eisenhamer, J., Dencheva, N., et al. 2022, JWST Calibration Pipeline, v1.6.2, Zenodo, doi:10.5281/zenodo.7041998  
 Cushing, M. C., Rayner, J. T., & Vacca, W. D. 2005, *ApJ*, 623, 1115  
 de Kok, R. J., Brogi, M., Snellen, I. A. G., et al. 2013, *A&A*, 554, A82  
 Encrenaz, T., Lellouch, E., Drossart, P., et al. 2004, *A&A*, 413, L5  
 Faedi, F., Barros, S. C. C., Anderson, D. R., et al. 2011, *A&A*, 531, A40  
 Feinstein, A. D., Radica, M., Welbanks, L., et al. 2023, *Natur*, 614, 670  
 Foreman-Mackey, D., Hogg, D. W., Lang, D., & Goodman, J. 2013, *PASP*, 125, 306  
 Giacobbe, P., Brogi, M., Gandhi, S., et al. 2021, *Natur*, 592, 205  
 Gibson, N. P., Merritt, S., Nugroho, S. K., et al. 2020, *MNRAS*, 493, 2215  
 Goorvitch, D. 1994, *ApJS*, 95, 535  
 Grant, D., & Wakeford, H. R. 2022, Exo-TiC/ExoTiC-LD: ExoTiC-LD v3.0.0, Zenodo, doi:10.5281/zenodo.7437681  
 Harris, C. R., Millman, K. J., van der Walt, S. J., et al. 2020, *Natur*, 585, 357  
 Hauschildt, P. H., Allard, F., & Baron, E. 1999, *ApJ*, 512, 377  
 Heng, K., & Lyons, J. R. 2016, *ApJ*, 817, 149  
 Hoeijmakers, H. J., Schwarz, H., Snellen, I. A. G., et al. 2018, *A&A*, 617, A144  
 Horne, K. 1986, *PASP*, 98, 609  
 Hoyer, S., & Hamman, J. 2017, *JORS*, 5, 10  
 Hoyer, S., Roos, M., Joseph, H., et al. 2022, xarray, v2022.03.0, Zenodo, doi:10.5281/zenodo.6323468  
 Hunter, J. D. 2007, *CSE*, 9, 90  
 Jakobsen, P., Ferruit, P., de Oliveira, C. A., et al. 2022, *A&A*, 661, A80  
 JWST Transiting Exoplanet Community Early Release Science Team, Ahrer, E.-M., Alderson, L., et al. 2023, *Natur*, 614, 649  
 Konopacky, Q. M., Barman, T. S., Macintosh, B. A., & Marois, C. 2013, *Sci*, 339, 1398  
 Kreidberg, L. 2015, *PASP*, 127, 1161  
 Li, G., Gordon, I. E., Rothman, L. S., et al. 2015, *ApJS*, 216, 15  
 Line, M. R., Brogi, M., Bean, J. L., et al. 2021, *Natur*, 598, 580  
 Lodders, K., & Fegley, B. 1998, *The Planetary Scientist's Companion*/Katharina Lodders, Bruce Fegley, (New York: Oxford Univ. Press)  
 Lodders, K., & Fegley, B. 2002, *Icar*, 155, 393  
 Lothringer, J. D., & Barman, T. S. 2020, *AJ*, 159, 289  
 Magic, Z., Chiavassa, A., Collet, R., & Asplund, M. 2015, *A&A*, 573, A90  
 Mancini, L., Esposito, M., Covino, E., et al. 2018, *A&A*, 613, A41  
 Miles, B. E., Biller, B. A., Patapis, P., et al. 2022, *ApJL*, 946, L6  
 Moré, J. J. 1978, *Numerical Analysis* (Berlin: Springer), 105  
 2022, pandas development team, T pandas-dev/pandas: Pandas v1.4.3, Zenodo, doi:10.5281/zenodo.6702671  
 Petit dit de la Roche, D. J. M., Hoeijmakers, H. J., & Snellen, I. A. G. 2018, *A&A*, 616, A146  
 Price-Whelan, A. M., Lim, P. L., Earl, N., et al. 2022, *ApJ*, 935, 167  
 Rustamkulov, Z., Sing, D. K., Mukherjee, S., et al. 2023, *Natur*, 614, 659  
 Savitzky, A., & Golay, M. 1964, *AnaCh*, 36, 1627  
 Schwarz, H., Brogi, M., De Kok, R., Birkby, J., & Snellen, I. 2015, *A&A*, 576, A111  
 Snellen, I., de Kok, R., Birkby, J. L., et al. 2015, *A&A*, 576, A59  
 Snellen, I. A. G., de Kok, R. J., de Mooij, E. J. W., & Albrecht, S. 2010, *Natur*, 465, 1049  
 Stevenson, K. B., Lewis, N. K., Bean, J. L., et al. 2016, *PASP*, 128, 094401  
 Tsai, S.-M., Lee, E. K. H., Powell, D., et al. 2022, *Natur*, 617, 483  
 Virtanen, P., Gommers, R., Oliphant, T. E., et al. 2020, *NatMe*, 17, 261  
 Welch, B. L. 1947, *Biometrika*, 34, 28  
 Zhang, M., Knutson, H. A., Wang, L., et al. 2021, *AJ*, 161, 181